

Compliant Metamaterials for Resonantly Enhanced Infrared Absorption Spectroscopy and Refractive Index Sensing

Imogen M. Pryce,[†] Yousif A. Kelaita,[†] Koray Aydin,[†] and Harry A. Atwater^{†,‡,*}

[†]Thomas J. Watson Laboratories of Applied Physics, MS 128-95, California Institute of Technology, Pasadena, California 91125, United States, and

[‡]Kavli Nanoscience Institute, MS 128-95, California Institute of Technology, Pasadena, California 91125, United States

The design of nanophotonic sensors has garnered increasing interest as nanoscale fabrication becomes more sophisticated. New fabrication capabilities, advances in nanoscale analysis, and the improved computational power of full-field electromagnetic simulations have led to a wealth of new designs based on the surface plasmon resonance of metallic structures. By tuning the geometrical properties of nanoscale features, shapes from crescents to bowtie antennas have achieved increasingly higher electric field enhancements, which translate to improved sensitivity.^{1–3} In recent years, optical metamaterials, which are metallodielectric composites made up of subwavelength elements, have emerged as a new class of nanostructured architectures that enable the control and directed emission of light.^{4–6} While nanostructured plasmonic designs exhibit a characteristic dielectric permittivity resonance, metamaterial designs offer in addition tunable optical frequency magnetic resonance, which is more sensitive to the environment and exhibits a narrower line width.⁷ This resonance can be tuned from the visible through the infrared by changing the geometry of a characteristic resonator, and the line width can be narrowed *via* coupling of metamaterial unit cells.⁸

A common approach to sensing is to detect small changes in the refractive index of the local environment by measuring the shift in frequency of the local surface plasmon resonance (LSPR).^{9–14} Plasmonic nanostructures have been used extensively as LSPR detectors since their resonant frequency is highly sensitive to changes in the dielectric constant of their environment. Typical wavelength and energy sensitivities

ABSTRACT Metamaterials can be designed to operate at frequencies from the visible to the mid-IR, making these structures useful for both refractive index sensing and surface-enhanced infrared absorption spectroscopy. Here we investigate how the mechanical deformation of compliant metamaterials can be used to create new types of tunable sensing surfaces. For split ring resonator based metamaterials on polydimethylsiloxane we demonstrate refractive index sensing with figures of merit of up to 10.1. Given the tunability of the resonance of these structures through the infrared after fabrication, they are well suited for detection of the absorption signal of many typical vibrational modes. The results highlight the promise of postfabrication tunable sensors and the potential for integration.

KEYWORDS: plasmonics · refractive index sensing · active metamaterials · polymers · surface-enhanced spectroscopy

are respectively in the hundreds to thousands of nm/RIU and tens to hundreds of meV/RIU. The highest reported values are for structures with sharp edges and coupled features with small interparticle gaps.^{15–19} Functionalization of the metallic surfaces can be used to limit binding to specific analytes, and this approach has been used to demonstrate a high degree of molecular sensitivity.²⁰

Complementary to refractive index sensors are surface-enhanced spectroscopic techniques, such as surface-enhanced Raman spectroscopy (SERS) and surface-enhanced infrared absorption (SEIRA), which are widely used for sensing particular biological and chemical agents. The sensitivity depends on the high electric field intensities of nanostructured surfaces leading to signal enhancement factors on the order of 10^8 and 10^4 – 10^5 for SERS and SEIRA, respectively.^{1,2,21–28} Similarly, the most sensitive SERS and SEIRA structures have sharp corners or edges, which support significant enhancements to the local electric field intensity, resulting in detection limits on

* Address correspondence to haa@caltech.edu.

Received for review July 25, 2011 and accepted September 19, 2011.

Published online September 19, 2011
10.1021/nn202815k

© 2011 American Chemical Society

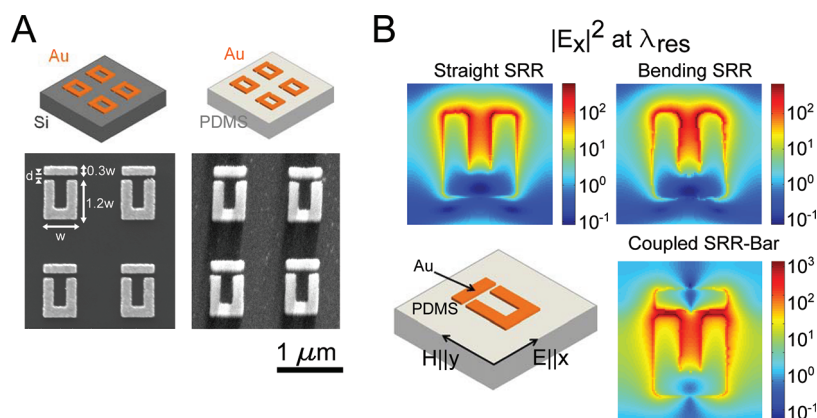


Figure 1. (A) SEM micrographs of a representative array of split ring resonators (SRRs) are shown both before and after transfer to the PDMS substrate. The schematics serve as labels for the micrographs. For the structures shown here, $w = 500$ nm, $d = 40$ nm, and the other dimensions scale as indicated with w . (B) The electric field intensity is plotted for three different resonator cases, each at their respective resonant frequency. The straight SRR case shows the simulated field for a basic uncoupled SRR. The bending SRR case includes the deformation of the SRR arms when the resonators are attached to a compliant substrate. The bottom right panel shows the coupled SRR-bar system, and the schematic at the bottom left shows the electric field polarization relative to an individual resonator.

the order of zeptomoles for SEIRA²⁵ and single-molecule spectroscopy using SERS substrates.^{29–31} SEIRA enhancements are weaker than those anticipated for SERS, as the SEIRA local field enhancement depends on $|E|^2$ versus $|E|^4$ for SERS. This combined with the difficulty of making a substrate that can operate over the entire infrared regime has led to far less research into SEIRA substrates. Metamaterial designs are well suited to this problem, as they can be designed to operate throughout the infrared spectral range and have both sharp edges and strong interfeature coupling required for high enhancement factors. There have been several previous demonstrations of both surface-enhanced and refractive index metamaterial-based sensors in the literature.^{14,25,32} By building metamaterial-based sensors that operate in the near to mid-IR, the molecular fingerprinting regime, the narrow magnetic resonance could be exploited to both sense changes in refractive index and enhance the signal of a particular vibrational mode.

Although metamaterials can be designed to work in any wavelength regime, their operating frequency is largely fixed by the constituent materials at the time of fabrication. Ideally the response would be tunable *in situ* to operate over a broader bandwidth and cover many different vibrational modes of the analyte. Here, we use a metamaterial system based on coupled splitting ring resonators (SRR) adhered to a polymeric substrate, polydimethylsiloxane (PDMS), to demonstrate precise control over resonant frequency tunability and electric field enhancement. The resonant frequency of an SRR, ω_0 , is described by $\omega_0 \approx 1/(LC)^{1/2}$, where L is the inductance and depends on the resonator path length and C is the capacitance across the split in the resonator. By integrating the resonators with a compliant substrate, mechanical deformation can be used to change the capacitance of the gap and the coupling

strength between resonators.^{32,33} This can be exploited to achieve up to line-width tunability of the resonant response and to customize the response of the metamaterial postfabrication. Here we present a metamaterial-based sensor that exploits the mechanical deformability of a highly compliant polymeric substrate to both detect small changes in refractive index and resonantly enhance the signal from several specific vibrational modes.

RESULTS AND DISCUSSION

The sensitivity of both refractive index sensors and surface-enhanced spectroscopic techniques depends critically on the intensity of the local electric field and its overlap with the analyte. We have previously shown that designing coupled resonator structures greatly enhances the local field at the resonant frequency, in a manner similar to the hybridization of plasmonic nanostructures.⁸ Thus, we start our discussion with an analysis of the calculated field enhancements for coupled resonators. The resonator geometries that we choose to utilize in this work are 100 nm thick Au SRRs coupled to Au bars (SRR-bar) on a PDMS substrate. As discussed in previous work,³² the metamaterials are fabricated by patterning Au resonators on a Si handle wafer (Figure 1A) and then transferring the patterns to a PDMS substrate using a hard/soft nanolithographic pattern transfer process. The SEM micrograph of the structures on PDMS (Figure 1A, right panel) shows the fidelity of the pattern transfer process for a representative array of SRRs with a resonator width (w) of 500 nm and a coupling distance (d) of 40 nm. For the resonators utilized in this work the SRR-bar aspect ratio remained constant as the dimensions were varied, as indicated in Figure 1A.

The electric field intensity for three different resonators on PDMS is calculated *via* full-field electromagnetic

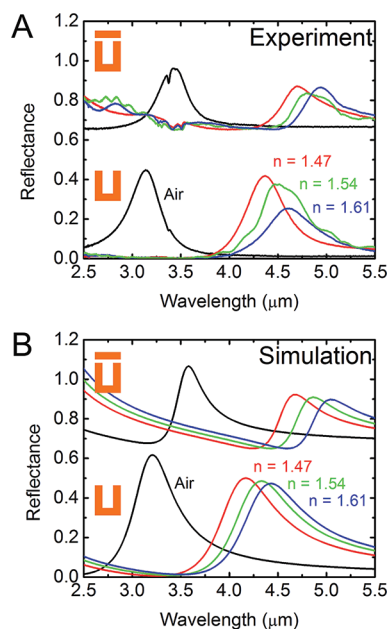


Figure 2. (A) Experimentally measured FTIR reflection spectra for representative arrays are shown. The bottom set of data are for an array of uncoupled resonators in air and three different optical matching fluids. The index of the fluids used is indicated in the plot. The coupled data are for an array of SRR-bar resonators with a coupling distance of 40 nm. The response for uncoupled and coupled arrays is also simulated, and these data are shown in (B).

simulation at their respective resonant frequencies with the electric field polarized perpendicular to the resonator arms (Figure 1B). In the top left panel, we show the electric field plot for an SRR with straight arms. This simulation uses the measured geometry of a resonator on Si as determined from SEM micrographs of the patterned Au. When uncoupled resonators are transferred to the PDMS substrate, however, the stress in the PDMS causes the arms to bend inward slightly. This bending causes an increase in the electric field intensity at the tips of the SRR, as made evident by the top right panel of Figure 1B, which increases the sensitivity of these structures compared to straight SRRs. In the bottom right panel, the coupled SRR-bar case is plotted. The coupling in this unit cell increases the maximum field intensity by an order of magnitude relative to the uncoupled case. Coupling resonators in a metamaterial unit cell is thus critical to the design of highly sensitive sensors or to any application that requires locally enhanced electromagnetic fields.

In order to further test the idea of using metamaterials as refractive index sensors, we consider first the SRR geometry shown in Figure 1 with $w = 500$ nm. We use FTIR spectroscopy to measure the reflectance of the arrays across the IR spectrum. The experimentally measured spectra for both an uncoupled SRR and a coupled SRR-bar with $d = 40$ nm are shown in Figure 2A. For clarity, we limit the width of the graph to the region where the magnetic resonant peak is located. We note that the electric resonance of the material is

blue-shifted from this peak. The resonance of the uncoupled SRR on PDMS in an ambient environment is $3.14 \mu\text{m}$, and coupling of an SRR to a bar shifts the resonant frequency to $3.42 \mu\text{m}$ (Figure 2A). In order to determine the sensitivity of the arrays as refractive index sensors, the reflection spectra were measured in three different index-matching fluids with refractive indices of 1.47, 1.54, and 1.61. The resonant frequency of the array is highly dependent on the dielectric constant of the surrounding environment, and increases cause the resonance to red-shift due to the increase in effective capacitance of the split gap. The resonance shifts from $4.37 \mu\text{m}$ in the $n = 1.47$ index-matching fluid to $4.61 \mu\text{m}$ in the $n = 1.61$ index-matching fluid. This represents a shift in the resonant wavelength, $\Delta\lambda_{\text{res}}$, from the initial measurement in air of 1.23 and $1.47 \mu\text{m}$, respectively. The resonant peak shifts are more dramatic for the $d = 40$ nm coupled resonator case, where the resonance is $4.71 \mu\text{m}$ in the $n = 1.47$ index-matching fluid and $4.94 \mu\text{m}$ in the $n = 1.61$ index-matching fluid, a red shift of 1.28 and $1.51 \mu\text{m}$, respectively. The simulated data for these resonator arrays are shown in Figure 2B. The uncoupled resonator data shown take into account the resonator bending described previously and enable a much better fit to the experimentally obtained values than the straight SRR case, which is not shown here.

From the reflectance data, we can calculate the sensitivities of the resonator arrays, defined as the change in resonant frequency as a function of change in refractive index in units of nm/RIU. The sensitivity is then divided by the full width at half-maximum (fwhm) of the resonant peak in an ambient environment to determine the figure of merit (FOM) of the resonator array.³⁴ We report FOM values for two different unit cell width geometries: 500 and 220 nm. A representative SEM micrograph of a 4×4 array of resonators on PDMS is shown (Figure 3A and D). For the larger, $w = 500$ nm, resonator array we calculate FOM values of up to 8.9 for a coupling distance of $d = 40$ nm and a slightly lower value of 8.2 for a coupling distance of 55 nm. The unfilled data point in Figure 3B where $d = 500$ nm refers to the uncoupled resonator case. Figure 3C shows corresponding simulation data for a number of different coupling distances, and we calculate FOM values of 6.0 and 5.4 for coupling distances of 40 and 60 nm, respectively. We attribute the lower FOM values to the broadening of the resonant peaks in simulation, as evident in Figure 2B. We simulate the SRR with both straight arms and with bending arms as previously described, and we find that the enhanced local field of the SRR while bending leads to an increase in the FOM from 3.3 to 3.7. The FOM values for the smaller resonator are higher than those reported for the larger unit cell, with values of 10.1 for a coupling distance of 30 nm and 9.3 for a coupling distance of 40 nm (Figure 3B). As in Figure 3B, we plot the FOM

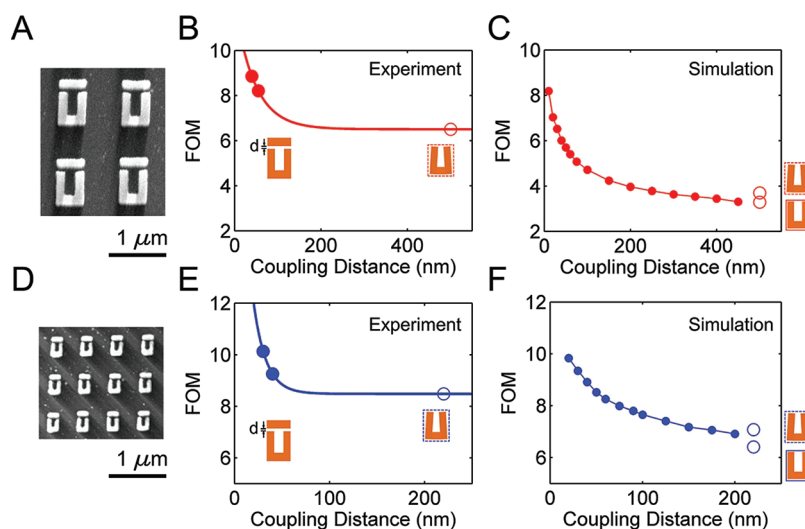


Figure 3. (A) Environmental SEM of representative structures on PDMS are shown. (B) Experimentally determined figure of merit (FOM) values of resonators with $w = 500$ nm are plotted. The FOM is the sensitivity in terms of nm/RIU divided by the full-width at half-maximum (fwhm) of the resonant peak in air. The unfilled data point at a coupling distance of 500 nm refers to the uncoupled SRR, *i.e.*, without a bar. (C) Simulated data for the same resonators are plotted. (D–F) Two different uncoupled resonator cases are simulated: the “straight SRR” and “bending SRR”. The same data for smaller resonators are shown in (D–F). Here, the uncoupled distance is equal to the width of the resonator, 220 nm.

TABLE 1. Summary of the Values Obtained for Different Sizes of Coupled and Uncoupled Resonators^a

structure (nm)	w (nm)	d (nm)	λ_{res} (μm)	sensitivity (nm/RIU)	sensitivity (meV/RIU)	fwhm (nm)	FOM
SRR	220		1.42	1192	497	141	8.5
SRR-bar	220	40	1.45	1225	488	121	10.1
SRR	500		3.14	2480	216	381	6.5
SRR-bar	500	40	3.33	2546	190	286	8.9
SRR	800		5.09	3366	116	521	6.5

^a Resonator width, w , and coupling distance, d , are used to define the resonator geometry. λ_{res} is the resonant wavelength in air, fwhm is the full width at half-maximum of the resonance peak in air, FOM is the figure of merit defined as sensitivity (nm/RIU)/fwhm (nm).

value of 8.5 for the uncoupled resonator at a coupling distance equal to the resonator width of 220 nm. The simulated values are also reported for a number of points, and we compute a FOM of 8.9 for $d = 40$ nm, 8.3 for $d = 60$ nm, and 7.1 for the uncoupled, bent SRR case.

Reducing the coupling distance between resonators leads to higher FOM as a result of the higher local electric field for both resonator sizes. In addition, we find that the FOM value will always be higher for a coupled resonator, as the presence of the bar narrows the resonant peak. We attribute part of the discrepancy between simulation and experiment to inaccurate modeling of the SRRs on PDMS and assume that the average degree of bending of the SRR arms is actually higher for the ensemble than that predicted by the single SRR unit cell used in simulation. It is also possible that the SRR arms bend inward when coupled to a bar, and this could also contribute differences for larger coupling distances where the stress is not offset by the

bar. Nevertheless, these FOM data represent the highest values reported for nanostructures in the IR compared to previous reports of 3.9 for Au structures.¹⁴ This design is rivaled only by a three-dimensional double nanopillar structure, which has a FOM of 23 at a resonant wavelength of 1368 nm.¹⁷

We summarize our experimental results in Table 1 and find that the highest FOM values can be engineered for the smallest coupling distances and the smallest resonator sizes. On the other hand, large SRRs are capable of achieving much higher sensitivity values (nm/RIU). One of the key features of this approach is that resonators can be designed to span a broad spectrum. We report the resonant wavelength of the structures on PDMS in an ambient environment for a number of different sized resonators in addition to their sensitivities and FOM values. The sensitivity in units of eV/RIU is also reported for comparison with other sensor geometries. The wide distribution of resonance values shows that resonators can be designed to work through most of the IR with limits being imposed, not by the fabrication technique or design stipulations, but rather by the characterization techniques available. For instance, the 800 nm SRR-bar geometry is not included in Table 1 because the resonance is red-shifted out of the range of the detector.

The ability to tune the response of these resonators either through fabrication or with *in situ* dynamic strain is also of interest for surface-enhanced spectroscopic techniques, where alignment to particular vibrational modes is crucial for enhancement of the molecular signal. For example, the dips in the experimental data in Figure 2A for the coupled resonator in air case (black

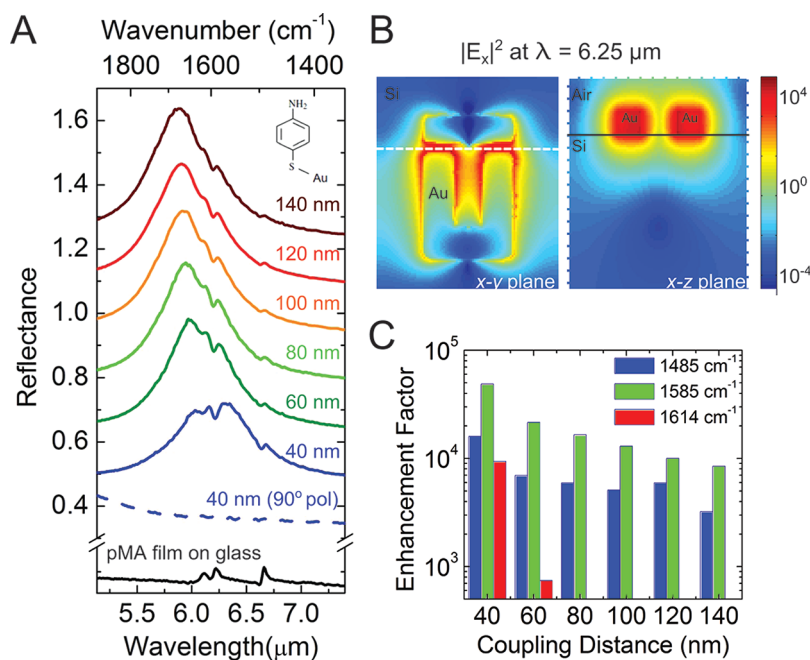


Figure 4. (A) FTIR reflection spectra data are shown for arrays of resonators on Si functionalized with pMA. The coupling distance is indicated in the labels. The dotted line shows cross-polarized data for the array at 40 nm coupling distance. The black line is the spectrum for an 800 nm thick film of pMA on glass. The structure of the pMA molecule is inset in the figure. The data are offset for clarity. (B) Electric field intensity at the resonant wavelength ($\lambda = 6.25 \mu\text{m}$) for the 40 nm coupled resonator system is plotted. The simulated data for both the x - y plane (left) and the x - z plane (right) are shown. The x - z plane is taken at the point indicated by the dotted line on the x - y plane panel. (C) The enhancement factor values for each vibrational mode signal are graphed as a function of coupling distance.

line) near $3.3 \mu\text{m}$ are due to an overlap of the metamaterial resonance with the vibrational modes of the symmetric and antisymmetric C–H stretch bonds in the PDMS. The notch in the uncoupled resonator in air peak is also due to these modes. In this work, we focus our attention on the IR absorption signals from the vibrational modes of *p*-mercaptoaniline (pMA) and show how they can be enhanced using coupled SRR-bar nanostructures.

First, we use arrays of coupled Au SRR-bar resonators on Si with unit cell widths of 500 nm and coupling distances from 40 to 140 nm. This static structure emulates the behavior that can be induced mechanically by integrating the resonators with a compliant substrate as the resonant frequency shifts from 6.0 to $6.3 \mu\text{m}$ over this range of coupling distances. The surface of the coupled resonators is functionalized with a monolayer of pMA by leaving the sample in a 10 mM ethanolic solution overnight. The thiol group on the pMA binds preferentially to the Au, and a monolayer is formed. The sample is then thoroughly rinsed with ethanol prior to measuring to ensure that only a monolayer remains bound to the surface of the Au. The pMA coverage was also confirmed using XPS measurements. The reflectance spectra after pMA functionalization are reported for each coupling distance (Figure 4A). We identify three peaks in the data corresponding to the $\delta\text{N-H}$ mode at $6.20 \mu\text{m}$ (1614 cm^{-1}), the $\nu\text{C-C}$ mode at $6.31 \mu\text{m}$ (1585 cm^{-1}), and the $\nu\text{C-C}$ and

$\delta\text{C-H}$ vibrational modes at $6.73 \mu\text{m}$ (1485 cm^{-1}) (ref 21). As the coupling distance changes, the resonant peak shifts through these frequencies and the overlap of the metamaterial resonance with each vibrational mode results in pronounced dips in the reflection spectra.

The enhancement of the vibrational mode signals can be calculated relative to an 800 nm thick reference film of pMA (Figure 4A, black line) and is dependent on the local field enhancement at the resonant peak. We first quantify the dip in the reflection spectra as the difference, ΔR_{SRR} , between the maximum and the minimum value of reflectance at each vibrational frequency. We find maxima of 4.5% for the C–C stretch bond at 1585 cm^{-1} , 1.7% for the N–H delta mode, and 1% for the mode at 1485 cm^{-1} . In order to confirm that the observed signals are due to enhanced electromagnetic fields at the metamaterial resonance, we also report the cross-polarized reflectance spectra for the $d = 40 \text{ nm}$ SRR-bar (Figure 4A, blue dotted line). We note that there are no observable peaks in this spectrum. This is corroborated by measurements (not shown here) of functionalized planar Au surfaces and arrays with resonant frequencies far from these vibrational modes where there is also no detectable pMA signal. The electric field intensity at $6.25 \mu\text{m}$ (1600 cm^{-1}) for both the x - y plane and the x - z plane of the $d = 40 \text{ nm}$ SRR-bar is shown in Figure 4B. The x - z plane cut is taken at a point just beyond the tips of the

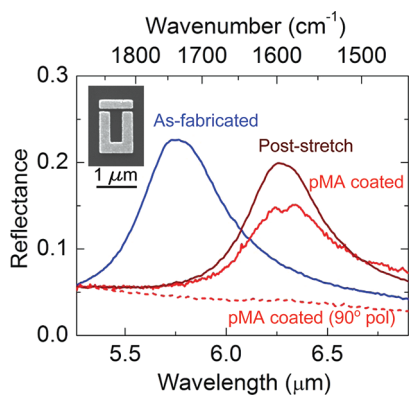


Figure 5. FTIR reflection spectra for an array of resonators on PDMS with a coupling distance of 60 nm are shown. The “As-fabricated” response for the resonator array is shown in blue, the dark red line shows the spectrum for the array of resonators after stretching to the appropriate resonance, and the red line indicates the response for the array after functionalizing with pMA. The dotted line shows the cross-polarized measurement for the functionalized array.

SRR arms, where the field intensity is highest (dotted white line). We note that the near-field enhancement is strongest through the gap and along the sides of the SRR and choose all regions with $|E_x|^2$ greater than 10^3 to determine the electromagnetic hot spot region. We assume monolayer coverage of pMA to the resonators and a molecular cross-section on Au of 0.3 nm^2 (ref 35). The signal enhancement factor (EF) for each vibrational mode is determined by comparing the ratios of the resonantly enhanced signals to the signals from the neat pMA according to $EF = (\Delta R_{\text{SRR}}/N_{\text{SRR}})/(\Delta R_{\text{ref}}/N_{\text{ref}})$, where N_{SRR} is the number of molecules adsorbed in the high-intensity region of the SRR, N_{ref} is the number of molecules contributing to the signal from the pMA film, and ΔR_{ref} is the signal for each vibrational mode. The EF values for the vibrational modes at each coupling distance are reported in Figure 4C. For the $d = 40 \text{ nm}$ SRR-bar array, we find SEIRA enhancement factors for all modes on the order of 10^4 , which is the same as other optimized nanostructured geometries.^{2,21} The high enhancement factors and the wide tunability of the approach enable access to any particular set of vibrational modes, indicating that metamaterial designs may be of particular interest to the development of new SEIRA, as well as SERS, substrates.

Although the enhancement factors for resonators on Si are high, this approach lacks the *in situ* tunability that may be possible with active metamaterial components. We also evaluate the coupled resonator metamaterials on PDMS as a potential SEIRA substrate. A major concern for this system, however, is the relatively low electric field intensity that is attainable. The electric field intensity observed for the SRRs on Si (Figure 4B) is an order of magnitude higher than that observed for the resonators on PDMS (Figure 1C) due to the much higher refractive index contrast of the Si with respect to the environment. The attractiveness of the PDMS

system is the tunability of the resonant response postfabrication, and we have previously shown that the metamaterial resonance can be tuned by a full line width *via* mechanical distortion of the substrate.³²

Here we use plastic deformation of the PDMS at the nanoscale to tune a resonator to the correct resonant frequency. We select an SRR-bar coupled resonator geometry with $w = 800 \text{ nm}$, $d = 40 \text{ nm}$ (Figure 5, inset), and an initial resonant frequency of $5.78 \mu\text{m}$ (Figure 5, blue line). The sample is stretched 25% parallel to the SRR arms, pulling the bar away from the SRR. When the strain is released, the PDMS between the resonators contracts, causing the coupling distance to decrease from the initial value. The resonant wavelength is permanently red-shifted to $6.27 \mu\text{m}$, which is evident from the FTIR reflection spectrum (Figure 5, dark red line). The new resonance coincides with the vibrational mode of interest in pMA at 1585 cm^{-1} , demonstrating how sensors with customizable responses can be designed with postfabrication tunability.

The pMA is adsorbed to the surface of the PDMS in a manner similar to that used in microcontact printing.³⁶ A drop of a 10 mM ethanolic solution of pMA is placed on the surface of the PDMS and allowed to dry. The sample is measured after drying, and an obvious dip is present in the center of the resonant peak (Figure 5, red line), which represents a ΔR of 0.9%. The cross-polarized data are also reported (red dashed line) and show that the molecular signal from the metamaterial substrate is due to the overlap of the metamaterial resonance and the pMA vibrational modes. The pMA signal was not apparent on bare patches of the PDMS or on arrays whose resonances did not overlap with the vibrational modes. We assume that a number of molecules, those adhered to the Au and those between the SRR and bar, contribute to the signal; however it is unclear exactly how many molecules contribute to the signal and will depend on the diffusion of pMA through the PDMS. Nevertheless, the observed signal for the pMA-coated sample is the first report of SEIRA from a compliant substrate and suggests that polymeric-based metamaterials could be useful platforms for sensing given both their *in situ* tunability and the potential for integration with polymeric-based devices, such as microfluidic cells. The signal from these types of sensors could be increased by using higher index polymeric substrates, making this approach a promising step forward in the design of flexible, tunable metamaterial-based sensors.

CONCLUSION

We have shown that compliant metamaterials can be used to sense changes in refractive index at a number of resonant frequencies with FOM values of up to 10.1. We have shown that resonator size can be used to tune the resonant frequency through the IR

and achieve sensitivities of 3370 nm/RIU (120 meV/RIU) for large resonators at long wavelengths and 1190 nm/RIU (500 meV/RIU) for small resonators in the near IR. We have also demonstrated that by coupling the metamaterial resonance to particular vibrational modes, we can enhance a vibrational mode signal with coupled Au resonators on Si by a factor of 10^4 . Resonators on a compliant substrate can be stretched and mechanically deformed in order to optimize the alignment

of a vibrational mode with the metamaterial resonant frequency postfabrication, and we note that vibrational modes at frequencies more than a line width distance from the as-fabricated resonance could be accessed by inducing substrate strain. Exploiting and tailoring the mechanical deformation of these metamaterial systems opens the door to the possibility of creating a new class of *in situ* customizable sensing surfaces.

EXPERIMENTAL METHODS AND MATERIALS

Sample Fabrication. The samples are fabricated using the hard/soft nanolithographic pattern transfer technique described in previous work.³² Arrays of 100 nm thick Au resonators are patterned *via* e-beam lithography on Si, with dimensions as shown in Figure 1A. Each array is 100 μm long by 100 μm wide. The Au is functionalized using 3-mercaptopropyl trimethoxysilane to improve adhesion to the polydimethylsiloxane. PDMS with increased elasticity is made using a ratio of 1:12 curing agent to prepolymer (Dow Corning Sylgard 184). The PDMS is cured for 1 h at 70 $^{\circ}\text{C}$ on the patterns, and a low-bias inductively coupled plasma reactive ion etch (ICP-RIE) with SF_6 is used to selectively remove the Si wafer, leaving a free-standing, 1 mm thick PDMS substrate with 100 nm thick metallic patterns (Figure 1B).

FTIR Measurements. The samples are measured between $\lambda = 1.5$ and 8 μm in a Fourier transform infrared (FTIR) microscope equipped with a liquid nitrogen cooled MCT detector. The measurements are taken in reflection mode at normal incidence and are the result of the coaddition of 64 scans with a 1.928 cm^{-1} resolution. A CaF_2 polarizer is placed in the incident beam path, and a KBr beamsplitter is used for all measurements. The reflectance data are normalized to a gold standard. The measurements are conducted with the light hitting the sample from the SRR or fluid side. For the fluid experiments, a MgO glass slide is used on top of the fluid surface. The refractive index environment was varied using Series A index-matching fluids from Cargille.

Simulation. Full-field electromagnetic wave calculations are performed using Lumerical, a commercially available finite-difference time-domain simulation software. A unit cell of the investigated structure is simulated using periodic boundary conditions along the x and y axes and perfectly matched layers along the propagation of electromagnetic waves (z axis). A broadband plane wave is incident on the unit cell along the $+z$ direction, and reflection is monitored by a power monitor that is placed behind the radiation source. Electric fields are monitored by frequency profile monitors. The optical constants for Au were taken from Palik, and a constant refractive index of 1.2 was used for the PDMS.

Calculating IR Signal Enhancement. We choose all regions in the simulated unit cell with $|E_x|^2$ greater than 10^3 to determine the active surface area. The path length of the high-intensity region is multiplied by the thickness of the Au, 100 nm, to give a surface area of 0.087 μm^2 . We assume monolayer coverage of pMA to the resonators and a molecular cross-section on Au of 0.3 nm^2 (ref 35), yielding approximately 4.4×10^8 active pMA molecules per SRR (N_{SRR}). Monolayer coverage of the Au SRRs was confirmed using XPS. The number of molecules contributing to the signal from the 800 nm thick pMA reference film is 1.2×10^{13} molecules (N_{ref}). We determine the enhancement factor: $\text{EF} = (\Delta R_{\text{SRR}}/N_{\text{SRR}})/(\Delta R_{\text{ref}}/N_{\text{ref}})$.

Stretching Compliant Sample and Customizing Resonant Frequency. A custom-built stage is used to induce tensile strain in the samples. Strain is defined as $l/l_0 \times 100\%$, where l_0 is the initial length of the sample array. This length is measured in the microscope and accurate to within 1%. The stage is mounted on

the FTIR microscope in order to measure the resonance at each strain and each “relaxed” or deformed state.

Acknowledgment. We acknowledge financial support from the Air Force Office of Scientific Research under grant FA9550-09-1-0673 and the Air Force Research Laboratory under grant FA8650-09-D-5037. I.M.P. acknowledges the support of a National Science Foundation Graduate Fellowship. We acknowledge critical support and infrastructure provided for this work by the Kavli Nanoscience Institute at Caltech. The authors thank Professor George Rossman for access to his IR facilities and useful discussion, Joseph Beardslee for performing XPS studies of control Au films, Ryan Briggs, Derrick Chi, Melissa Melendes, and Christos Santis for help with reactive ion etching of the sample, and Vivian Ferry and Emily Warmann for useful discussions.

REFERENCES AND NOTES

- Lal, S.; Grady, N. K.; Kundu, J.; Levin, C. S.; Lassiter, J. B.; Halas, N. J. Tailoring Plasmonic Substrates for Surface Enhanced Spectroscopies. *Chem. Soc. Rev.* **2008**, *37*, 898–911.
- Bukasov, R.; Shumaker-Parry, J. S. Silver Nanocrescents with Infrared Plasmonic Properties As Tunable Substrates for Surface Enhanced Infrared Absorption Spectroscopy. *Anal. Chem.* **2009**, *81*, 4531–4535.
- Bukasov, R.; Ali, T. A.; Nordlander, P.; Shumaker-Parry, J. S. Probing the Plasmonic Near-Field of Gold Nanocrescent Antennas. *ACS Nano* **2010**, *4*, 6639–6650.
- Shalaev, V. M. Optical Negative-Index Metamaterials. *Nat. Photonics* **2007**, *1*, 41–48.
- Smith, D. R.; Pendry, J. B.; Wiltshire, M. C. K. Metamaterials and Negative Refractive Index. *Science* **2004**, *305*, 788–792.
- Dolling, G.; Enkrich, C.; Wegener, M.; Zhou, J. F.; Soukoulis, C. M. Cut-Wire Pairs and Plate Pairs as Magnetic Atoms for Optical Metamaterials. *Opt. Lett.* **2005**, *30*, 3198–3200.
- Linden, S.; Enkrich, C.; Wegener, M.; Zhou, J. F.; Koschny, T.; Soukoulis, C. M. Magnetic Response of Metamaterials at 100 Terahertz. *Science* **2004**, *306*, 1351–1353.
- Aydin, K.; Pryce, I. M.; Atwater, H. A. Symmetry Breaking and Strong Coupling in Planar Optical Metamaterials. *Opt. Express* **2010**, *18*, 13407–13417.
- Dong, Z. G.; Liu, H.; Cao, J. X.; Li, T.; Wang, S. M.; Zhu, S. N.; Zhang, X. Enhanced Sensing Performance by the Plasmonic Analog of Electromagnetically Induced Transparency in Active Metamaterials. *Appl. Phys. Lett.* **2010**, *97*, 114101.
- McFarland, A. D.; Van Duyne, R. P. Single Silver Nanoparticles as Real-Time Optical Sensors with Zeptomole Sensitivity. *Nano Lett.* **2003**, *3*, 1057–1062.
- Nehl, C. L.; Liao, H. W.; Hafner, J. H. Optical Properties of Star-Shaped Gold Nanoparticles. *Nano Lett.* **2006**, *6*, 683–688.
- Underwood, S.; Mulvaney, P. Effect of the Solution Refractive-Index on the Color of Gold Colloids. *Langmuir* **1994**, *10*, 3427–3430.
- Tam, F.; Moran, C.; Halas, N. J. Geometrical Parameters Controlling Sensitivity of Nanoshell Plasmon Resonances

- to Changes in Dielectric Environment. *J. Phys. Chem. B* **2004**, *108*, 17290–17294.
14. Liu, N.; Weiss, T.; Mesch, M.; Langguth, L.; Eigenthaler, U.; Hirscher, M.; Sonnichsen, C.; Giessen, H. Planar Metamaterial Analogue of Electromagnetically Induced Transparency for Plasmonic Sensing. *Nano Lett.* **2010**, *10*, 1103–1107.
 15. Hao, F.; Sonnefraud, Y.; Van Dorpe, P.; Maier, S. A.; Halas, N. J.; Nordlander, P. Symmetry Breaking in Plasmonic Nanocavities: Subradiant LSPR Sensing and a Tunable Fano Resonance. *Nano Lett.* **2008**, *8*, 3983–3988.
 16. Hao, F.; Nordlander, P.; Sonnefraud, Y.; Van Dorpe, P.; Maier, S. A. Tunability of Subradiant Dipolar and Fano-Type Plasmon Resonances in Metallic Ring/Disk Cavities: Implications for Nanoscale Optical Sensing. *ACS Nano* **2009**, *3*, 643–652.
 17. Kubo, W.; Fujikawa, S. Au Double Nanopillars with Nanogap for Plasmonic Sensor. *Nano Lett.* **2011**, *11*, 8–15.
 18. Kottmann, J. P.; Martin, O. J. F.; Smith, D. R.; Schultz, S. Non-Regularly Shaped Plasmon Resonant Nanoparticle as Localized Light Source for Near-Field Microscopy. *J. Microsc. (Oxford, U. K.)* **2001**, *202*, 60–65.
 19. Klar, T.; Perner, M.; Grosse, S.; von Plessen, G.; Spirkl, W.; Feldmann, J. Surface-Plasmon Resonances in Single Metallic Nanoparticles. *Phys. Rev. Lett.* **1998**, *80*, 4249–4252.
 20. Liu, J. P.; Eddings, M. A.; Miles, A. R.; Bukasov, R.; Gale, B. K.; Shumaker-Parry, J. S. In Situ Microarray Fabrication and Analysis Using a Microfluidic Flow Cell Array Integrated with Surface Plasmon Resonance Microscopy. *Anal. Chem.* **2009**, *81*, 4296–4301.
 21. Kundu, J.; Le, F.; Nordlander, P.; Halas, N. J. Surface Enhanced Infrared Absorption (SEIRA) Spectroscopy on Nanoshell Aggregate Substrates. *Chem. Phys. Lett.* **2008**, *452*, 115–119.
 22. Wang, H.; Kundu, J.; Halas, N. J. Plasmonic Nanoshell Arrays Combine Surface-Enhanced Vibrational Spectroscopies on a Single Substrate. *Angew. Chem., Int. Ed.* **2007**, *46*, 9040–9044.
 23. Le, F.; Brandl, D. W.; Urzhumov, Y. A.; Wang, H.; Kundu, J.; Halas, N. J.; Aizpurua, J.; Nordlander, P. Metallic Nanoparticle Arrays: A Common Substrate for Both Surface-Enhanced Raman Scattering and Surface-Enhanced Infrared Absorption. *ACS Nano* **2008**, *2*, 707–718.
 24. Neubrech, F.; Pucci, A.; Cornelius, T. W.; Karim, S.; Garcia-Etxarri, A.; Aizpurua, J. Resonant Plasmonic and Vibrational Coupling in a Tailored Nanoantenna for Infrared Detection. *Phys. Rev. Lett.* **2008**, *101*, 157403.
 25. Cubukcu, E.; Zhang, S.; Park, Y. S.; Bartal, G.; Zhang, X. Split Ring Resonator Sensors for Infrared Detection of Single Molecular Monolayers. *Appl. Phys. Lett.* **2009**, *95*, 043113.
 26. Jensen, T. R.; Van Duyne, R. P.; Johnson, S. A.; Maroni, V. A. Surface-Enhanced Infrared Spectroscopy: A Comparison of Metal Island Films with Discrete and Nondiscrete Surface Plasmons. *Appl. Spectrosc.* **2000**, *54*, 371–377.
 27. Osawa, M.; Ataka, K.; Yoshii, K.; Nishikawa, Y. Surface-Enhanced Infrared Spectroscopy – The Origin of the Absorption Enhancement and Band Rule in the Infrared-Spectra of Molecules Adsorbed on Fine Metal Particles. *Appl. Spectrosc.* **1993**, *47*, 1497–1502.
 28. Adato, R.; Yanik, A. A.; Amsden, J. J.; Kaplan, D. L.; Omenetto, F. G.; Honge, M. K.; Erramilli, S.; Altug, H. Ultra-Sensitive Vibrational Spectroscopy of Protein Monolayers with Plasmonic Nanoantenna Arrays. *Proc. Natl. Acad. Sci. U. S. A.* **2009**, *106*, 19227–19232.
 29. Nie, S. M.; Emery, S. R. Probing Single Molecules and Single Nanoparticles by Surface-Enhanced Raman Scattering. *Science* **1997**, *275*, 1102–1106.
 30. Xu, H. X.; Bjerneld, E. J.; Kall, M.; Borjesson, L. Spectroscopy of Single Hemoglobin Molecules by Surface Enhanced Raman Scattering. *Phys. Rev. Lett.* **1999**, *83*, 4357–4360.
 31. Kneipp, K.; Wang, Y.; Kneipp, H.; Perelman, L. T.; Itzkan, I.; Dasari, R.; Feld, M. S. Single Molecule Detection Using Surface-Enhanced Raman Scattering (SERS). *Phys. Rev. Lett.* **1997**, *78*, 1667–1670.
 32. Pryce, I. M.; Aydin, K.; Kelaita, Y. A.; Briggs, R. M.; Atwater, H. A. Highly Strained Compliant Optical Metamaterials with Large Frequency Tunability. *Nano Lett.* **2010**, *10*, 4222–4227.
 33. Huang, F.; Baumberg, J. J. Actively Tuned Plasmons on Elastomerically Driven Au Nanoparticle Dimers. *Nano Lett.* **2010**, *10*, 1787–1792.
 34. Sherry, L. J.; Jin, R. C.; Mirkin, C. A.; Schatz, G. C.; Van Duyne, R. P. Localized Surface Plasmon Resonance Spectroscopy of Single Silver Triangular Nanoprisms. *Nano Lett.* **2006**, *6*, 2060–2065.
 35. Mohri, N.; Matsushita, S.; Inoue, M.; Yoshikawa, K. Desorption of 4-Aminobenzenethiol Bound to a Gold Surface. *Langmuir* **1998**, *14*, 2343–2347.
 36. Kumar, A.; Whitesides, G. M. Features of Gold Having Micrometer to Centimeter Dimensions Can be Formed Through a Combination of Stamping with an Elastomeric Stamp and an Alkanethiol Ink Followed by Chemical Etching. *Appl. Phys. Lett.* **1993**, *63*, 2002–2004.